



저작자표시-비영리-변경금지 2.0 대한민국

이용자는 아래의 조건을 따르는 경우에 한하여 자유롭게

- 이 저작물을 복제, 배포, 전송, 전시, 공연 및 방송할 수 있습니다.

다음과 같은 조건을 따라야 합니다:



저작자표시. 귀하는 원저작자를 표시하여야 합니다.



비영리. 귀하는 이 저작물을 영리 목적으로 이용할 수 없습니다.



변경금지. 귀하는 이 저작물을 개작, 변형 또는 가공할 수 없습니다.

- 귀하는, 이 저작물의 재이용이나 배포의 경우, 이 저작물에 적용된 이용허락조건을 명확하게 나타내어야 합니다.
- 저작권자로부터 별도의 허가를 받으면 이러한 조건들은 적용되지 않습니다.

저작권법에 따른 이용자의 권리는 위의 내용에 의하여 영향을 받지 않습니다.

이것은 [이용허락규약\(Legal Code\)](#)을 이해하기 쉽게 요약한 것입니다.

[Disclaimer](#)

Thesis for the Degree of Master of Engineering

An analysis of bidirectional
reflectance distribution function
(BRDF) with field goniometer system
based on multispectral camera of
unmanned aerial vehicle (UAV)

by

Minji Kim

Division of Earth Environmental System Science

(Major of Spatial Information Engineering)

The Graduate School

Pukyong National University

February, 2023

An analysis of bidirectional reflectance
distribution function (BRDF) with field
goniometer system based on multispectral
camera of unmanned aerial vehicle (UAV)
(무인항공기(UAV)의 다중분광 카메라
기반 현장 각도계 시스템을 이용한
양방향 반사율 분포 함수(BRDF) 분석)

Advisor: Prof. Chul Uong Choi

by
Minji Kim

A thesis submitted in partial fulfillment of the requirements
for the degree of

Master of Engineering

in Division of Earth Environmental System Science
(Major of Spatial Information Engineering),
The Graduate School, Pukyong National University

February 2023

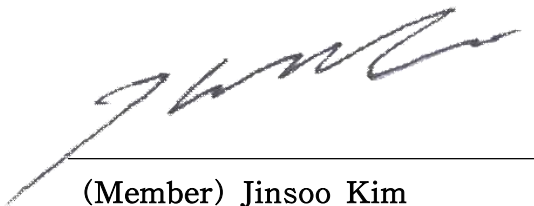
An analysis of bidirectional reflectance distribution function
(BRDF) with field goniometer system based on multispectral
camera of unmanned aerial vehicle (UAV)

A dissertation
by
Minji Kim

Approved by:



(Chairman) Yangwon Lee



(Member) Jinsoo Kim



(Member) Chul Uong Choi

February 17, 2023

Table of Contents

I. Introduction	1
1. Background of Research	1
A. The Conception of BRDF	2
B. The Purpose of Estimating BRDF in Remote Sensing	3
C. BRDF Models	3
D. Goniometer	4
2. The Purpose of Research	5
II. Materials and Method	7
1. Research Data Collection	7
A. Research Target	7
B. Equipment for Research Data Collection and Software	8
(1) P4 Multispectral	8
(2) D-RTK 2	11
(3) GRX2	12
(4) Spectroradiometer	14
(5) GS pro	16
C. Data Collection	16

(1) Creation of a hemispherical flight course for BRDF estimation	16
(2) Hemispherical image acquisition	21
2. Data Preprocessing	22
3. Orthomosaic and Orthophoto Creation	23
A. Photogrammetry Program: Agisoft Metashape	23
B. Method to Create Orthophotos	24
4. Research Data Analysis	25
A. Metadata Extraction	25
B. DN Extraction	26
C. Calculate the Reflectance of the Target in the Images	26
D. ANIF Calculation	27
E. Calculation of k value of BRDF	28
III. Results and Discussion	31
1. Calculation of Reflectance of the Target	31
A. Measured Irradiance Results	31
(1) The irradiance data from P4 Multispectral sunlight sensor	31
(2) The irradiance data from spectroradiometer with RCR	33
B. Calculation of Reflectance of Each Tarps	34
2. BRDF Estimation and Analysis	35

A. ANIF Calculation	35
B. Calculation of the k value of the BRDF Model	38
C. Homogeneity Analysis to Determine tarp Accuracy	43
IV. Conclusion	44
V. References	46



List of Tables

Table 1	Specification of P4 Multispectral	9
Table 2	The specification of RTK equipped on P4 Multispectral	11
Table 3	Specification of GRX2	13
Table 4	Input value of azimuth and zenith angle of check images	19
Table 5	The hemispherical flight information for BRDF sampling	22
Table 6	The reflectance of tarps calculated using spectroradiometer data 34	
Table 7	The reflectance of tarps from UAV images calculated using irradiance data measured by spectroradiometer with RCR (unit: %)	35
Table 8	The k value of BRDF model calculated in this study	39
Table 9	The difference between simulated reflectance and calculated reflectance before and after irradiance correction (unit: %)	40
Table 10	The uncertainty of each tarps according to homogeneously ..	43

List of Figures

Figure 1 The flowchart of this study	6
Figure 2 The site of fieldwork and the tarps installed on the site	8
Figure 3 P4 Multispectral	9
Figure 4 The spectral characteristics of P4 Multispectral camera	10
Figure 5 D-RTK 2	12
Figure 6 Location of ground control points(GCPs)	13
Figure 7 The spectroradiometer attached a remote cosine receptor(RCR) on the ground	14
Figure 8 The spectral white reference(WR) and spectroradiometer	15
Figure 9 The spectroradiometer measuring radiance of tarps	16
Figure 10 Hemisphere flight course. (a) bird's eye view (b) side view.18	
Figure 11 Check flight course. (a) bird's eye view (b) side view.	20
Figure 12 The flowchart of making orthophotos in Metashape	24
Figure 13 The irradiance value for each band measured by sunlight sensor of P4 Multispectral	31
Figure 14 The comparison of irradiance data from P4 Multispectral sunlight sensor and attitude of P4 Multispectral	32
Figure 15 The irradiance for al band measured by spectroradiometer with RCR	33
Figure 16 The templete of ANIF result polar plot	36
Figure 17 The ANIF results before and after irradiance correction	37
Figure 18 The ANIF results simulated by BRDF model estimated after	

irradiance correction 42



무인항공기(UAV)의 다중분광 카메라 기반 현장 각도계 시스템을 이용한 양방향 반사율 분포 함수(BRDF) 분석

김 민 지

부경대학교 대학원 공간정보시스템공학전공

요 약

양방향 반사율 분포 함수(BRDF)는 지표면의 비등방성 반사 특성을 태양과 센서의 위치의 기하학적 관계로 설명하는 함수로서 인공위성 영상이나 항공사진이 연직 아래 방향으로 지표면을 관측하지 않았을 때 발생하는 양방향 반사 효과를 보정하는 데 쓰일 수 있다. BRDF는 주로 현장에서 수집한 데이터를 기반으로 추정되는데, 데이터 수집에 쓰였던 기존의 현장 고니오미터 시스템은 매우 큰 크기와 무거운 무게를 가지고 있고, 반구형 데이터를 수집하는 데 오랜 시간이 걸린다는 단점이 있다. 이에 작고 가벼우며, 데이터를 수집하는 데 단 11분이면 충분한 UAV 고니오미터 시스템을 제안한다. 본 연구에서는 현장 실험을 통해 BRDF 데이터를 수집하였다. 현장 실험 장소에 4종의 타프를 설치하고, 각 타프를 대상으로 총 5회에 걸쳐 P4 Multispectral로 다중분광 영상을 수집하였다. 영상에서 타프의 반사율을 계산하는 데 필요한 복사 조도를 P4 Multispectral 상단의 sunlight sensor, 그리고 지상에 설치한 분광계를 통해 측정하였다. 밴드별 영상에서 타프의 반사도를 산정하는 데 P4 Multispectral의 sunlight sensor로 측정된 값보다 지상에서 측정된 값을 활용하는 것이 더욱 정확하였다. 이는 P4 Multispectral이 영상을 수집하면서 UAV의 자세를 바꾸었기 때문이다. 각 영상에 지상 irradiance 보정 유무에 따라 생성한 orthophoto를 통해 타프의 반사율을 계산하고, 이를 anisotropy factor(ANIF) 값으로 정규화한 뒤, BRDF 모델의 k 계수를 산정하였다. irradiance 보정을 한 영상으로 BRDF를 추정하였을 때가 보정을 하지 않았을 때보다 더 적은 표준편차를 보였다. UAV 고니오미터를 통해 BRDF를 추정한 결과는 기존의 고니오미터를 활용한 결과와 비슷한 정확도를 보였지만, 지상으로 입사하는 복사 조도 데이터가 필수적이다.

I. Introduction

1. Background of Research

Since the invention of unmanned aerial vehicles (UAVs), many researchers have actively used UAVs in various fields. In particular, rotary-wing UAVs are capable of vertical take-off and landing as well as hovering because their propellers directly rotate to generate lift. Meanwhile, fixed-wing UAVs require a relatively large space for take-off because the airfoil that generates lift is fixed to the aircraft. Therefore, rotary-wing UAVs are preferred over fixed-wing UAVs when hovering in a designated location is required, or when the research area is relatively narrow.

Satellite images or aerial photographs have been mainly used to observe the Earth through remote sensing, facilitating monitoring of vast areas from high altitudes; however, they have low spatial resolution. As UAVs can be operated only at an altitude of 150 m or less from the ground, UAV images have higher spatial resolution than satellite images and aerial photographs—UAVs have recently been used in various fields related to remote sensing because of this advantage. With the advent of UAVs equipped with multispectral sensors, as real-time spectroscopic observation of ground targets has become easier, various studies are being conducted on the analysis of spectroscopic characteristics of plants

in precision agriculture and their use in satellite image correction(Aebischer *et al.*, 2020; Jain and Pandey, 2021; Narmilan *et al.*, 2022; Sakamoto *et al.*, 2022; Zhou *et al.*, 2022).

When monitoring the Earth using satellites or UAVs, it is necessary to understand the reflection distribution characteristics of the ground surface or the observation target(Schopfer *et al.*, 2007). As the ground surface has an anisotropic reflection characteristic, the digital number (DN) in multi-angle observation appears different depending on the positional relationship between the sun and the sensor(Yeom *et al.*, 2005). The anisotropic reflection characteristic of a surface is an inherent property of a material(Sandmeier and Itten, 1999; Schopfer *et al.*, 2007). Acquired images cannot be utilized unless these effects are corrected or understood. The concept that emerged from this is the bidirectional reflectance distribution function (BRDF)(Huang *et al.*, 2013).

Many studies have utilized goniometers to sample the BRDF data. In this study, a UAV was used in a field experiment for data sampling for the BRDF analysis, to overcome the limitations of the existing goniometers in the field. Four tarps with different reflectance were installed on the ground, and by observing through the multi-spectral camera of the UAV, the reflectance distribution characteristics according to each band were analyzed based on the reflectance of targets.

A. The Conception of BRDF

The BRDF describes directional reflection by quantifying the distribution

of energy incident on a surface when it is reflected in a specific direction (Sandmeier and Itten, 1999; Maignan *et al.*, 2004). This concept is a function that describes the geometric reflective properties of most surfaces, which was named by Nicodemus (Nicodemus *et al.*, 1977; Huang *et al.*, 2013). The BRDF predicts the direction and signal of a surface reflection based on *a priori* information, when observing a surface from multiple angles (Huang *et al.*, 2013).

B. The Purpose of Estimating BRDF in Remote Sensing

Sensors on past satellites, such as SPOTs, collected data from the nadir at the same time each day. Thus, unlike the data acquired by current satellite sensors, the incident energy was sensed similar. However, MODIS of and Terra or MISR of Terra do not acquire data only from the nadir; therefore, the acquired data are inevitably affected by the anisotropic reflectance characteristics of the ground surface (Jensen and Schill, 2000). Therefore, the BRDF enables analysis of the reflectance characteristics of the acquired image by the sensor, by describing the geometric relationship between solar irradiance and the sensor.

C. BRDF Models

The utilization of multi-angle reflectance data has grown with the increased use of satellites. Consequently, several BRDF models have developed, including those based on semi-empirical kernels, such as the

one proposed by Roujean(Roujean *et al.*, 1992). This study used a linear combination model of isotropic, volumetric, and geometric scatterings, based on the Roujean model. The Li-Transit kernel, which has better efficiency at high SZA and VZA, was used as the geometric kernel, and the Ross-Thick-Maignan (RTM) kernel was used as the volume scattering kernel(Gao *et al.*, 2000; Maignan *et al.*, 2004; Jia *et al.*, 2020).

D. Goniometer

A goniometer is used for positioning a sensor at a desired azimuth and zenith angle. As it enables collecting data in a hemispherical shape, it is mainly used to collect hemispherical spectral data by attaching a spectroradiometer. Goniometers have been used as a reference system for angles in many studies(Sandmeier and Itten, 1999; Schill *et al.*, 2004). As the significance of the BRDF has recently emerged in the field of remote sensing, it is widely used to sample data to be used in BRDF-related research(Sandmeier and Itten, 1999; Painter *et al.*, 2003; Schill *et al.*, 2004; Dangel *et al.*, 2005; Schopfer *et al.*, 2007; Roosjen *et al.*, 2012). Traditionally used field goniometers are bulky and slow to collect data (Roosjen *et al.*, 2012). Field goniometers that are primarily used for the BRDF data collection include the Portable Apparatus for Rapid Acquisition of Bidirectional Observation of the Land and Atmosphere (PARABOLA) (Privette *et al.*, 1997; Vierling *et al.*, 1997; Abdou *et al.*, 2001), Sandmeier Field Goniometer (SFG)(Jensen and Schill, 2000; King *et al.*, 2001; Coburn and Peddle, 2006), Goniometer for Outdoor Portable Hyperspectral Earth

Reflectance (GOPHER)(Doctor *et al.*, 2015; Bachmann *et al.*, 2016), Gonio Radiometric Spectrometer System (GRASS)(Marks *et al.*, 2015; Bialek *et al.*, 2016), University of Lethbridge Goniometer System (ULGS)(Berry *et al.*, 2012; Bruegge *et al.*, 2019; Byford and Coburn, 2022).

A robot goniometer was developed to overcome the limitations of the traditional field goniometer(Roosjen *et al.*, 2012; Bihlmaier *et al.*, 2016). It collects data quicker than conventional goniometers, but its use is limited to laboratory data collection.

2. The Purpose of Research

This study attempted to overcome the disadvantages of the field goniometer, which is a classical means of sampling the BRDF data. A field goniometer has low mobility because of its bulky size, and low efficiency because of slow data collection. Therefore, research was conducted on improving mobility and efficiency in collecting hemispherical data, using a UAV goniometer. By designing a UAV capable of precise positioning to fly in a hemispherical shape, data were collected relatively quickly. Additionally, multi-spectral data were collected using the multi-spectral camera attached to the UAV, and the reflectance distribution characteristics for each band were analyzed. The coefficients of the BRDF were estimated from data collected by the UAV goniometer, and the accuracy of the BRDF was evaluated.

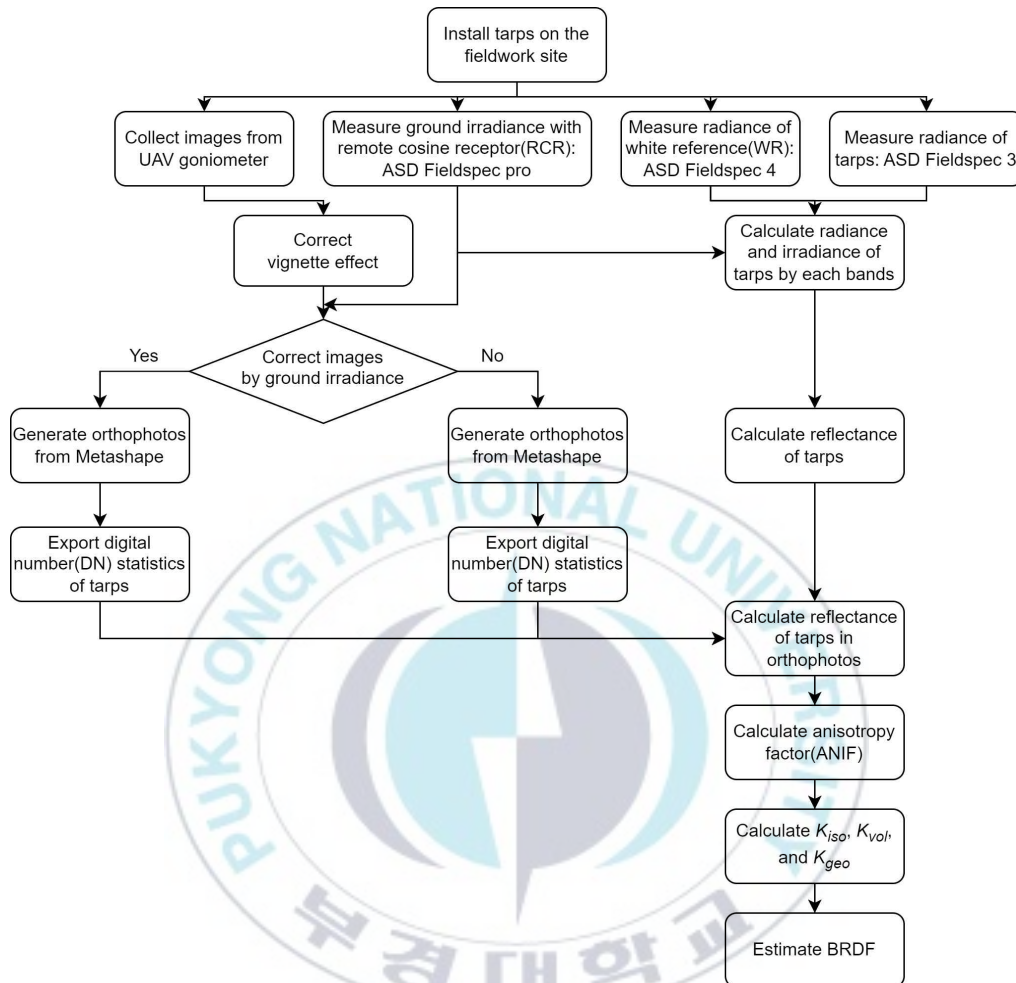


Figure 1 The flowchart of this study

II. Materials and Method

1. Research Data Collection

A. Research Target

The field experiment for this study was conducted at the driving test site of the Department of Agricultural Engineering Department, Rural Development Administration, Jeonju-si, Jeollabuk-do, from 28 to 29 October 2021. Four types of tarps with specific reflectance were installed at the selected site—the reflectance of the tarps were 3%, 21%, 31%, and 46%, respectively. Their size was approximately 15 m × 15 m. Figure 2 is the image taken by the UAV of the research site where the tarp was installed.



Figure 2 The site of fieldwork and the tarps installed on the site

B. Equipment for Research Data Collection and Software

(1) P4 Multispectral

In this study, multispectral images were collected using the P4 Multispectral—an agricultural UAV manufactured by DJI. Figure 3 shows the P4 Multispectral and Table 1 shows its specifications(DJI, 2022a).



Figure 3 P4 Multispectral

Table 1 Specification of P4 Multispectral

Takeoff Weight	1486g
Max Speed	31m/h
Max Flight Time	27 minutes
Operating Temperature	0 to 40°C
Operating Frequency	2.4000 GHz to 2.4835 GHz
Ground Sample Distance (GSD)	(H/18.9) cm/pixel
Sensors	1/2.9" CMOS
Effective pixels	2.08MP (2.12MP in total)
Field of View (FOV)	62.7°
Focal Length	5.74mm
Aperture	f/2.2
RGB Sensor ISO Range	200-800
Monochrome Sensor Gain	1 - 8x
Electronic Global Shutter	1/100 - 1/20000 s (visible light)
	1/100 - 1/10000 s (multispectral)
Image Size	1600 × 1300

In Table 1, H of (H/18.9) implies flight altitude (unit: m).

The P4 Multispectral is equipped with multispectral cameras corresponding to a total of six bands. It also has an automatic gimbal system that enables maintaining and adjusting the camera attitude. The spectral characteristics of the P4 Multispectral camera are shown in Figure 4.

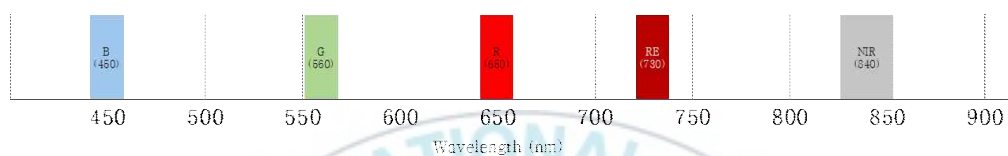


Figure 4 The spectral characteristics of P4 Multispectral camera

The P4 Multispectral is equipped with a sunlight sensor, which measures irradiance from the UAV itself and stores the measurement data as a signal value in the image metadata.

It is equipped with an RTK module as well as a sunlight sensor, enabling precise positioning in the image collection. The specifications of the built-in RTK module are shown in Table 2(DJI, 2022a).

Table 2 The specification of RTK equipped on P4 Multispectral

Frequency	GPS: L1/L2 GLONASS: L1/L2 BeiDou: B1/B2 Galileo[2]: E1/E5
First-Fixed Time	less than 50 s
Positioning Accuracy	Vertical 1.5 cm + 1 ppm (RMS) Horizontal 1 cm + 1 ppm (RMS)
Velocity Accuracy	0.03 m/s

In Table 2, 1 ppm implies that the error increases by 1 mm when moving 1 km.

When operating a UAV, there are several ways to receive RTK signals. In Korea, RTK signals can be received through the network RTK service provided by the National Geographic Information Institute. also, DJI D-RTK2 receiver can be used. In this study, RTK signals were received through the D-RTK 2 receiver that was installed as a base station.

(2) D-RTK 2

The D-RTK 2 is GNSS receiver of DJI. It can serve as a base station as the UAVs of DJI with RTK modules provide real-time positioning data with centimeter-level positioning accuracy. Figure 5 shows the D-RTK 2 used in this study.



Figure 5 D-RTK 2

(3) GRX2

To select ground control points(GCPs) in the study area, coordinate data of a specific location were obtained using a GNSS receiver: GRX2 of SOKKIA; its specifications are shown in Table 3.

Table 3 Specification of GRX2

Number of Channels	226
Tracked Signals	GPS, Glonass, Galileo, SBAS
Accuracy (RTK)	H: 10mm + 1ppm
	V: 15mm + 1ppm
Communication Ports	Bluetooth, Serial, SD/SDHD
Wireless Communication	Bluetooth, UHF, GSM/HSPA, CDMA
Dust/Water Protection	IP67
Size	Dia. 184 × H95mm
Weight: GRX2/BDC70 battery	1kg / 195g
Operating Temperature (with BDC70)	-20 to +65C
Operating Time	> 7.5 hours in static mode with Bluetooth Operation

The location of the GCP coordinates obtained through GRX2 is shown in Figure 6.



Figure 6 Location of ground control points(GCPs)

(4) Spectroradiometer

A spectroradiometer was installed to measure the irradiance, radiance, and reflectance of the target. The equipment was used in three different ways to collect data for each purpose. All spectroradiometers used below are Fieldspec from ASD(Westborough, MA, USA.)

(a) Measuring irradiance incident on the ground: ASD FieldSpec pro with RCR

The remote cosine receptor (RCR) measures the total amount of all energy incident on a hemispherical shape. Accordingly, the RCR enables a spectroradiometer to measure the total irradiance incident on a hemispherical shape. Therefore, to measure the irradiance of the sun incident on the ground, a spectroradiometer was installed along with the RCR on the ground; the installed equipment is shown in Figure 7.



Figure 7 The spectroradiometer attached a remote cosine receptor(RCR) on the ground

(b) Measurement of radiance reflected from the ground: ASD
Fieldspec 4 measuring WR

Radiance was measured using a spectral white reference(WR) as a target to obtain the total amount of energy incident on the ground and reflected. Figure 8 shows the installation of WR and ASD Fieldspec.



Figure 8 The spectral white reference(WR) and spectroradiometer

(c) Measuring the reflectance of a target with constant reflectance:
ASD Fieldspec 3

The reflectance distribution characteristics were analyzed for a target with constant reflectance, which was used in this study. To calculate the reflected energy of each target and its reflectance, the reflected energy was measured on the target with a spectroradiometer. Figure 9 shows the ASD Fieldspec 3, which measures the target and its reflected energy.



Figure 9 The spectroradiometer measuring radiance of tarps

(5) GS pro

UAVs are also automatically operated using dedicated software. The P4 Multispectral used in this study automatically flies along the course designed through the application provided by DJI, called GS pro.

C. Data Collection

(1) Creation of a hemispherical flight course for BRDF estimation

Multispectral images for the BRDF sampling were acquired by operating the UAV in a hemispherical shape based on the center of the tarp. The method of operating the UAV in a hemispherical shape and taking images is as follows. The latitude and longitude coordinates of the place where the tarp is installed are set. The position of the UAV is calculated based on the two data points, using formulas expressed in Equations (1) to (3).

$$x = lat + r \times \sin \phi \times \cos \theta \quad (1)$$

$$y = lon + r \times \cos \phi \times \cos \theta \quad (2)$$

$$z = r \times \sin \theta \quad (3)$$

where x is the latitude coordinate of the location of UAV, y is the longitude coordinate, and z is the altitude. Additionally, lat is the latitude coordinate of the center of the designated tarp, and lon is the longitude coordinate of the center. Each latitude and longitude coordinate is expressed as a decimal number. r is the radius of the hemisphere. As 1° is approximately 100 km in the set latitude and longitude coordinates, the radius of the desired hemisphere is entered in m units and divided by 10^5 to convert the unit. ϕ is the azimuth angle, and θ is the absolute value of the camera pitch angle.

The positional coordinates of a total of 150 hemispherical flight courses are calculated using the above formula. A total of 151 location coordinates are calculated by adding the location coordinates at an azimuth angle (ϕ) of 180° and a pitch angle (θ) of 90° for the nadir shooting. This enables creating hemispherical flight courses. Figure 10 shows the calculated coordinates of 151 locations.

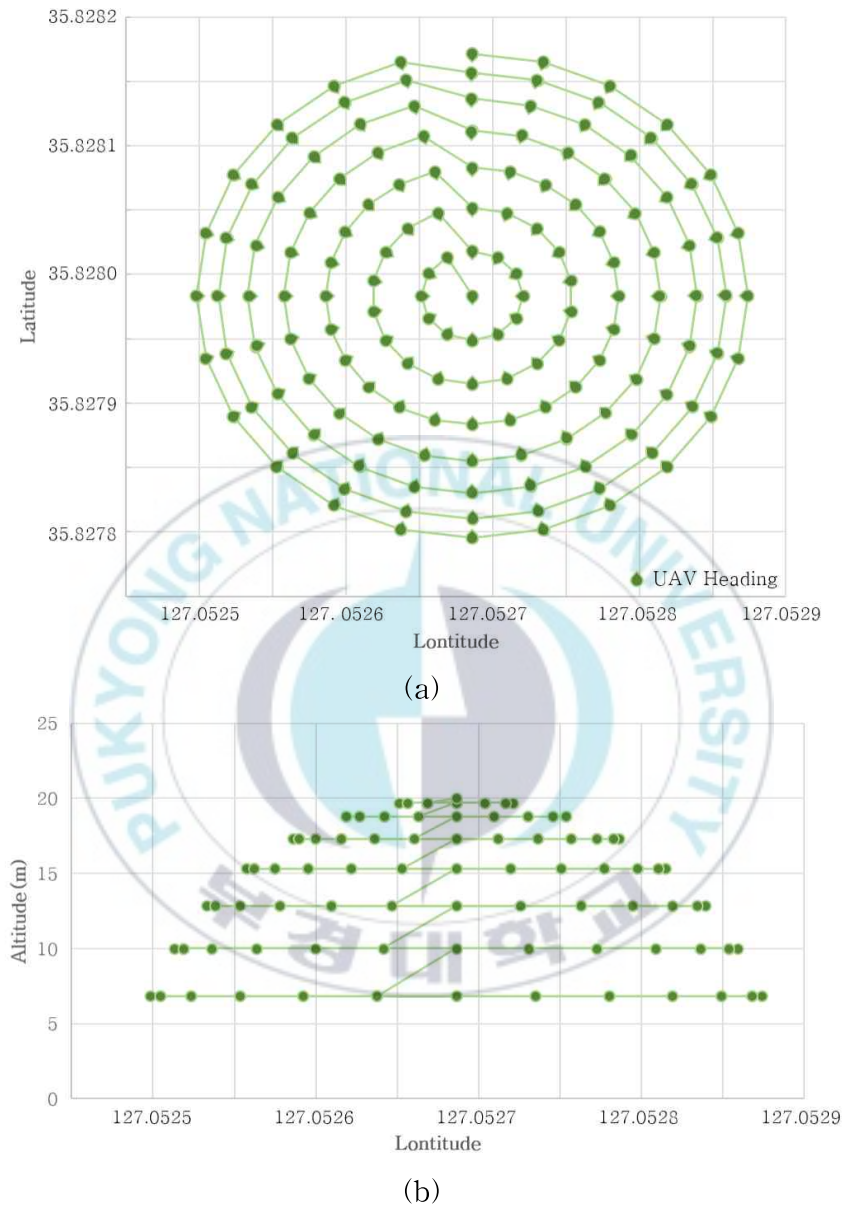


Figure 10 Hemisphere flight course. (a) bird's eye view (b) side view.

Check images were also acquired to examine the accuracy of the image obtained through hemispherical flight. The positions of the check images

are calculated through Equations (4) to (5). The locations of the calculated check images are shown in Figure 9.

$$x_c = lat + r \times \cos \phi' \times \tan (90 - \theta') \quad (4)$$

$$y_c = lon + r \times \sin \phi' \times \tan (90 - \theta') \quad (5)$$

Here, x_c is the latitude of the UAV location for the check image, and y_c is the longitude. Altitude (z) is omitted because it is equal to the radius. ϕ' is the azimuth angle of the UAV that captured the check image, and θ' is the absolute value of the camera pitch angle. The values entered for each variable are shown in Table 4. Figure 10 shows the positions of the 44 check images calculated accordingly.

Table 4 Input value of azimuth and zenith angle of check images

	Minimum	Maximum	Interval
ϕ'	78	348	90
θ'	57	87	3

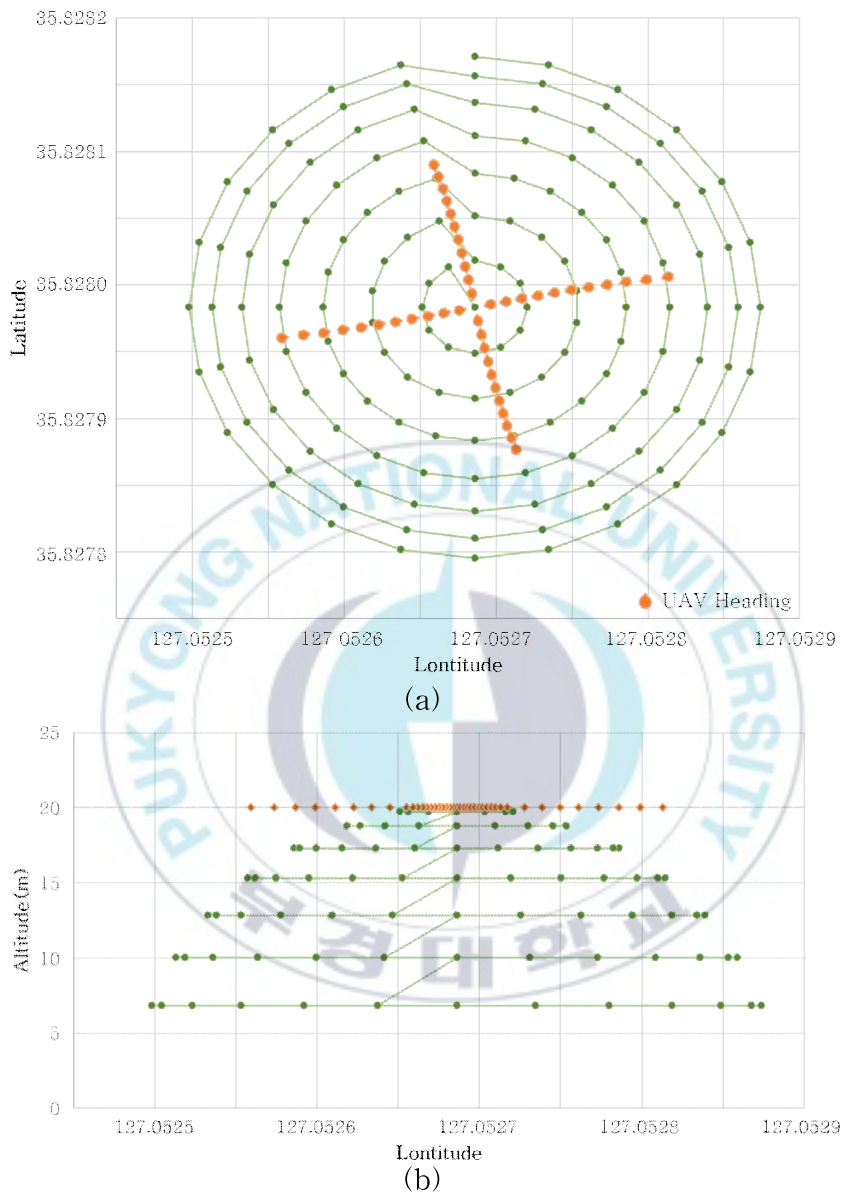


Figure 11 Check flight course. (a) bird's eye view (b) side view.

The calculated location data is saved in the Excel file format, then converted to the keyhole markup language (KML) format, which is used

to display geographic data in map-related browsers such as Google Earth and Google Maps. The KML uses a tag-based structure with nested elements and attributes and is based on extensible markup language (XML) standards. The converted KML file is input into GS Pro. The flight mission is created in GS Pro based on the KML file, but only the position data is entered, not the attitude data. Therefore, as previously designed, the attitude information of the UAV is input at each location. After entering all attitude information, the mission is saved.

(2) Hemispherical image acquisition

GS Pro is an application that operates UAV of DJI according to the planned mission. Through GS Pro, the previously created flight course is created as a mission and the P4 Multispectral is operated. The P4 Multispectral take images toward the target from a designated location and simultaneously measures irradiance through the equipped sunlight sensor. The hemispherical flight was conducted five-times, and a total of four targets were photographed. The related status is described in Table 5, including Flight name, Flight start time, Flight duration, Sun azimuth angle (SAA) and Sun zenith angle (SZA) for each flight, Reflectance of targets, and Number of images.

Table 5 The hemispherical flight information for BRDF sampling

Flight name	Start time (h:m:s)	Flight duration (m:s)	Sun azimuth angle	Sun zenith angle	Reflectance of targets	Number of images
1st-3%	10:03:21	11:01	142.6	57.8	3%	975
2nd-46%	10:17:11	11:03	146.2	56.1	46%	975
3rd-23%	10:31:45	11:01	149.9	54.6	23%	975
4th-46%	11:11:29	11:02	161.3	52.3	46%	975
5th-31%	12:08:23	11:07	179.2	49.3	31%	975

The P4 Multispectral is operated according to the created mission, collecting images. The P4 Multispectral camera has a total of six bands – images of six bands can be obtained with one shot. Therefore, 195 images by combining 151 hemispherical images and 44 check images were generated from six band images, and 975 images were obtained per flight.

2. Data Preprocessing

The images taken with the P4 Multispectral were preprocessed through a program using Python, which is a set of image processing formulas provided by DJI(DJI, 2022b). The vignetting can be found in the P4 Multispectral image, in which the brightness decreases from the center to the edge of an image(Kim and Pollefeys, 2008; Zheng *et al.*, 2009). It is expressed by Equations (6) and (7).

$$V(X, Y) = I(X, Y) \times (k_5 \times r^6 + k_4 \times r^5 + k_3 \times r^4 + k_2 \times r^3 + k_1 \times r^2 + k_0 \times r + 1.0) \quad (6)$$

$$r = \sqrt{(X - X_c)^2 + (Y - Y_c)^2} \quad (7)$$

where $V(X, Y)$ is a DN obtained by removing vignetting from image coordinates (X, Y) , and $I(X, Y)$ is a normalized DN. As the image of P4 Multispectral is a 16-bit, the DN of each image can be normalized by dividing 65535 values (DJI, 2022b). r is the distance between the pixel with image coordinates (X, Y) and the center pixel of the vignetting (X_c, Y_c) . The coordinates of (X_c, Y_c) for each image of each band can be checked in the metadata.

3. Orthomosaic and Orthophoto Creation

A. Photogrammetry Program: Agisoft Metashape

In this study, Agisoft Metashape program was used to process the UAV-collected data. Metashape is a photogrammetry program that uses the structure from motion (SfM) algorithm in which data to be modeled can be processed in parallel; thus, it has strength in processing voluminous data (Creasy *et al.*, 2021; Tinkham and Swayze, 2021).

To analyze the BRDF results based on a target with constant reflectance, an orthophoto of each image was created using Metashape. An orthophoto is an individual image in which undulation displacement or

radial distortion that can occur in aerial photographs is eliminated. An orthomosaic is a single image created without geometric distortion by mosaicking individual images(Smith, 1995).

B. Method to Create Orthophotos

Figure 11 shows the process of creating orthophotos on Metashape, from the received aerial photographs(P4 Multispectral images).

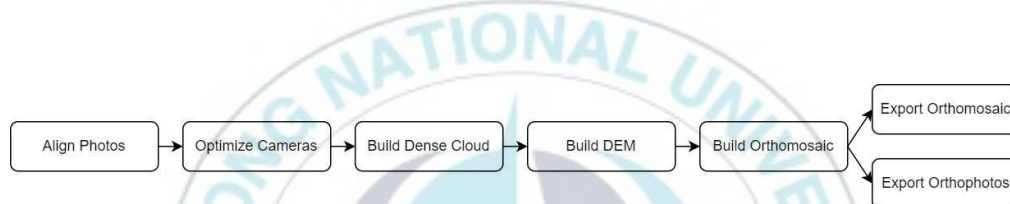


Figure 12 The flowchart of making orthophotos in Metashape

After performing all orthomosaic-generation steps, orthophotos can be created by correcting distortion. The image is geometrically corrected using the GCP obtained in the process of generating orthophotos. Data can be analyzed by extracting images at each location as orthophotos, and converting the DN of each image into reflectance in the orthophotos.

4. Research Data Analysis

A. Metadata Extraction

P4 Multispectral images include exchangeable image file format (EXIF), which is metadata containing image information. As the data necessary for image processing is included in the metadata, metadata is extracted through the open source Exiftool: elements of internal orientation, elements of exterior orientation, irradiance, GPS data, image center coordinates, camera attitude, etc.

Interior orientation (IO) refers to the process of determining the location of the reference point, lens distortion, principal point and focal length of the photo, and correcting errors and converting them into image coordinates (Jae-Hong *et al.*, 2006; Jeong *et al.*, 2015; Yu *et al.*, 2017). Accordingly, the elements of interior orientation include the focal length, principal point, and camera lens distortion coefficient. Exterior orientation (EO) refers to the process of transforming image coordinates into a required coordinate system. The elements of exterior orientation include the spatial position (X, Y, Z) where the image was captured and the attitude of the camera (roll, pitch, yaw) (Gašparović and Jurjević, 2017).

Irradiance data is the signal value input through the sunlight sensor of P4 Multispectral. Additionally, metadata stores latitude, longitude, and altitude data measured through the RTK module of P4 Multispectral, and information such as the coordinates of the center of the P4 Multispectral image and camera attitude when the image is captured can be known.

B. DN Extraction

The resulting orthophotos are free from geometric distortion; therefore, the DN of tarps can be extracted. After extracting the DN of each pixel of the image for each band, the average of DN per band was calculated, and later converted into energy and used to calculate the reflectance of the tarps.

C. Calculate the Reflectance of the Target in the Images

For BRDF estimation, the reflectance of the tarps must be calculated in the UAV images. After acquiring the UAV images, the energy was calculated based on the DN of the image of a tarp photographed in the direction of the nadir. DN was converted into an energy value based on the reflectance of the tarps measured with a spectroradiometer. After calculating the energy from the images, the ground irradiance was corrected by the correction factor calculated based on the average of the data measured by the spectroradiometer with RCR. The reflectance was calculated as in Equation (8) through the energy data of each image before and after ground irradiance correction.

$$\rho_{p4m} = \frac{L_{reflected}}{L_{incident}} = L_{p4m} \times \frac{\lambda_{camera}}{\lambda_{irradiance}} \times C_{p4m} \quad (8)$$

where ρ_{p4m} is the reflectance of the image, $L_{reflected}$ is the DN of the image, $L_{incident}$ is the DN value of the incident energy, L_{p4m} is the normalized DN of the image, λ_{camera} is the DN at the corresponding wavelength (λ), and $\lambda_{irradiance}$ is the irradiance signal value at the corresponding wavelength (λ) to be. C_{p4m} is the ground irradiance correction factor. λ_{camera} .

$$\lambda_{camera} = \frac{(L_{\lambda} - L_{Blacklevel}) \times V(X, Y)}{g \times \frac{\lambda_{etime}}{1e6}} \quad (9)$$

L_{λ} is the normalized DN at the corresponding wavelength (λ) to be, and $L_{Blacklevel}$ is the normalized black level DN. The black level of P4 Multispectral image is specified in the metadata as 4096. g is the sensor gain, λ_{etime} is the exposure time.

D. ANIF Calculation

The anisotropy factor (ANIF) is a factor that normalizes the reflectance at other locations based on the reflectance at the nadir. The BRDF data is affected by the spectral reflectance variability of the target; therefore, it is estimated using the ANIF because the reflectance of each image can be adjusted to the same index regardless of the reflectance value of the target. Thus, to intuitively understand the reflectance distribution characteristics of each tarp, all reflectance data were normalized by the

ANIF of each target(Sandmeier *et al.*, 1998). Equation (10) is the formula for calculating the ANIF(Sandmeier and Itten, 1999).

$$ANIF(\theta_s, \theta_v, \phi_s, \phi_v) = \frac{R_b(\theta_s, \theta_v, \phi_s, \phi_v)}{R_{nadir}(\theta_s, 0, \phi_s, 0)} \quad (10)$$

where θ_s is the SZA, θ_v is the vehicle zenith angle (VZA), ϕ_s is the SAA, and ϕ_v is the vehicle azimuth angle (VAA). R_b is the reflectance factor at each position, and R_{nadir} is the reflectance factor at the nadir.

E. Calculation of k value of BRDF

Based on the Roujean model, this study used a mixed model by adopting the Li Sparse-Reciprocal (LSR) kernel, Li Dense Reciprocal (LDR) kernel, Li-Transit kernel, and Ross-Thick-Maignan (RTM) kernel(Roujean *et al.*, 1992). The basic formula of the Roujean model is given in Equation (11)(Maignan *et al.*, 2004; Jiang and Li, 2008; Zhang *et al.*, 2018; Chang *et al.*, 2021).

$$\rho(\theta_s, \theta_v, \Delta\phi) = k_{iso} + k_{vol} \times f_{vol}(\theta_s, \theta_v, \Delta\phi) + k_{geo} \times f_{geo}(\theta_s, \theta_v, \Delta\phi) \quad (11)$$

$$\Delta\phi = |\phi_s - \phi_v|$$

$\rho(\theta_s, \theta_v, \Delta\phi)$ is the reflectance at the corresponding position. The Roujean model comprises k values and f values, in which f_{iso} , f_{vol} , and f_{geo} are coefficients of isotropic scattering, volume scattering, and geometric

scattering, respectively. After obtaining the f value based on the acquired data, the k value, which is the weight of each kernel, must be estimated through the relational expression. Once the k value is estimated, the reflectance at each position at any time can be obtained, thereby understanding the reflectance distribution characteristics of the target. In this study, the k value was calculated using Equations (12) to (20) (Gao *et al.*, 2000; Bréon *et al.*, 2002; Maignan *et al.*, 2004; Jiao *et al.*, 2016; Zhang *et al.*, 2018; Jia *et al.*, 2020).

$$f_{vol} = \frac{(\frac{\pi}{2} - \zeta) \times \cos \zeta + \sin \zeta}{\cos \theta_v + \cos \theta_s} \times (1 + (1 + \frac{\zeta}{\zeta_0})^{-1}) - \frac{\pi}{4} \quad (12)$$

$$\cos \zeta = \cos \theta_s \cos \theta_v + \sin \theta_s \sin \theta_v \cos \Delta \phi \quad (13)$$

$$f_{geo} = \begin{cases} f_{LiSR}, B \leq 2 \\ f_{LiDR} = \frac{2}{B} \times f_{LiSR}, B \geq 2 \end{cases} \quad (14)$$

$$f_{LiSR} = O(\theta'_s, \theta'_v, t) - \sec \theta'_s - \sec \theta'_v + \frac{1}{2}(1 + \cos \zeta') \times \sec \theta'_s \times \sec \theta'_v \quad (15)$$

$$B = \sec \theta'_s + \sec \theta'_v - O(\theta'_s, \theta'_v, \Delta \phi) \quad (16)$$

$$O(\theta'_s, \theta'_v, t) = \frac{1}{\pi}(t - \sin t \times \cos t) \times (\sec \theta'_s + \sec \theta'_v) \quad (17)$$

$$\theta'_v = \tan^{-1}(\frac{b}{r} \tan \theta_v); \theta'_s = \tan^{-1}(\frac{b}{r} \tan \theta_s) \quad (18)$$

$$\cos t = \frac{h}{b} \times \frac{\sqrt{D^2 \times \tan \theta'_s \times \tan \theta'_v \times \sin \Delta \phi}}{\sec \theta'_s + \sec \theta'_v} \quad (19)$$

$$D = \sqrt{\tan^2 \theta'_s + \tan^2 \theta'_v + 2 \times \tan \theta'_s \times \tan \theta'_v \times \cos \Delta \phi} \quad (20)$$

where ζ is the phase angle. f_{LiSR} and f_{LiDR} are values calculated with Li Sparse-Reciprocal (LSR) and Li Dense Reciprocal (LDR) kernels (Wanner *et al.*, 1995) developed from the Roujean model. In Equations (18) and (19), $\frac{b}{r}$ and $\frac{h}{b}$ are entered as 1 and 2, respectively, and ζ_0 is entered as 1.5° (Jia *et al.*, 2020).



III. Results and Discussion

1. Calculation of Reflectance of the Target

A. Measured Irradiance Results

(1) The irradiance data from P4 Multispectral sunlight sensor

Figure 12 shows the irradiance data for each band measured by the spectral sunlight sensor of the P4 Multispectral. The spectral range of irradiance data for each band is the same as that of the camera.

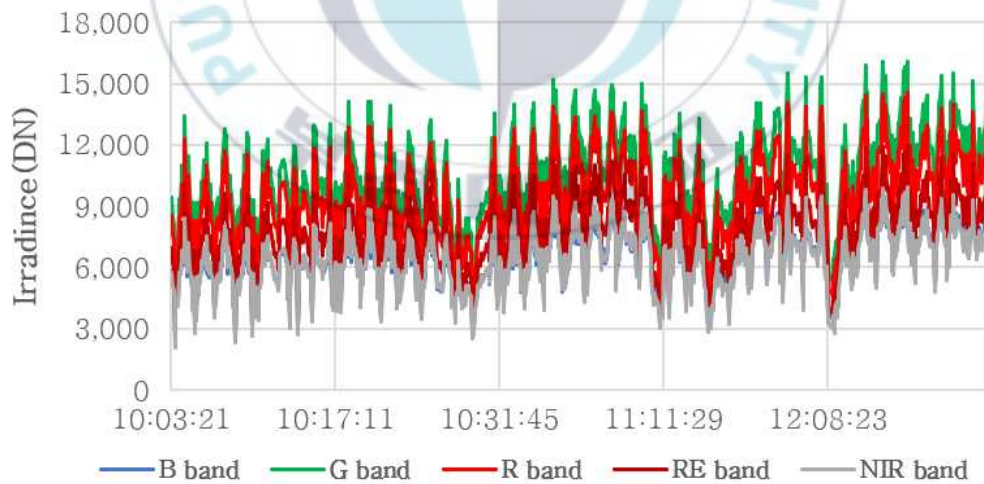


Figure 13 The irradiance value for each band measured by sunlight sensor of P4 Multispectral

Irradiance data presented different values for each band, but showed similar tendencies. According to Figure 13, irradiance significantly varies from minute to minute. However, as the solar energy incident on the ground does not change as the measured data, the reason why the data appears different from the general pattern was analyzed. Figure 14 shows the irradiance data measured by the sunlight sensor of the P4 Multispectral and the attitude of the P4 Multispectral, that is, VAA, when shooting a 3% tarp.

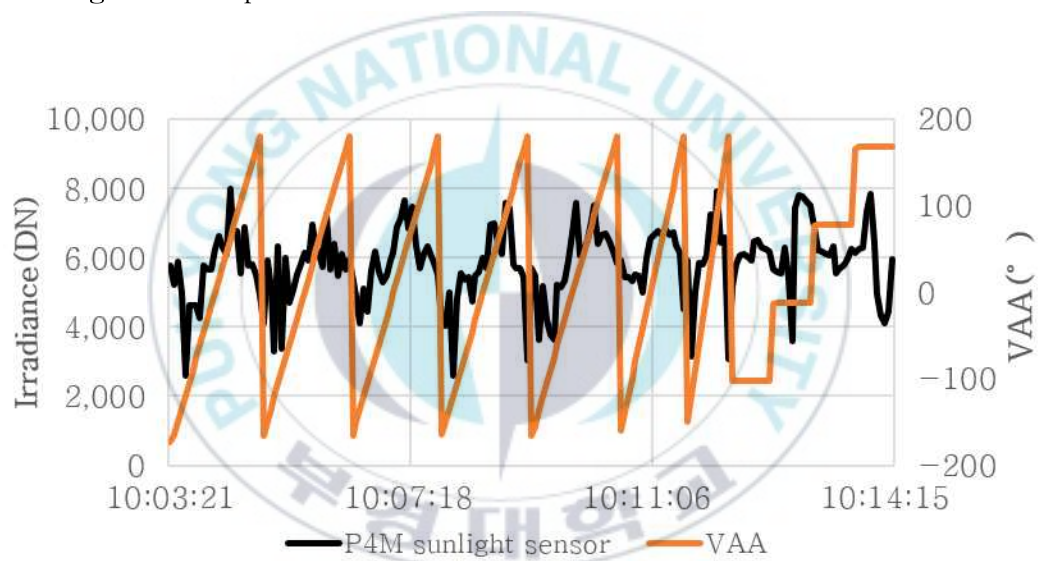


Figure 14 The comparison of irradiance data from P4 Multispectral sunlight sensor and attitude of P4 Multispectral

Figure 14 shows that the irradiance DN value measured by the sunlight sensor and the changing pattern of the P4 Multispectral attitude are similar. This indicates that the energy incident on the sunlight sensor affects the attitude of the P4 Multispectral.

(2) The irradiance data from spectroradiometer with RCR

Figure 13 shows the irradiance data measured by ASD Fieldspec pro with RCR. ASD Fieldspec pro can measure energies from 350nm to 2500nm. Figure 15 shows the irradiance data of all bands from 300nm to 2500nm.

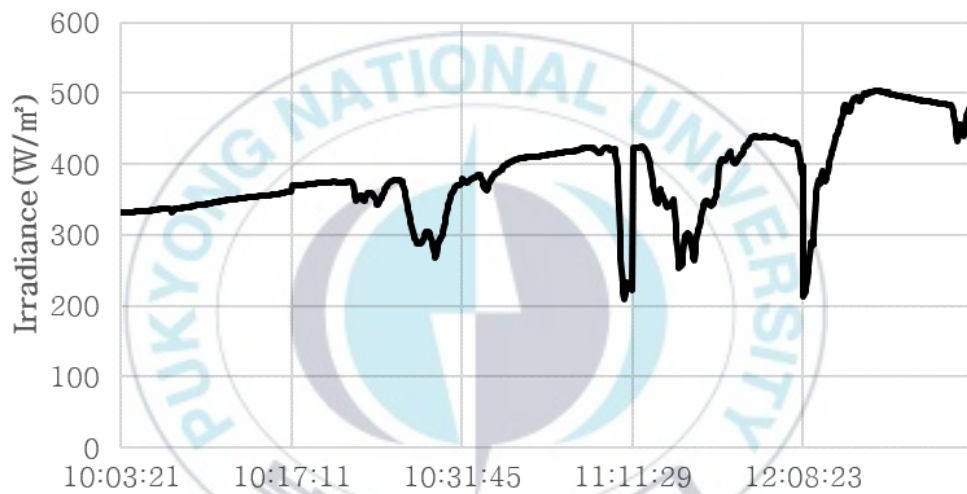


Figure 15 The irradiance for all band measured by spectroradiometer with RCR

The irradiance in all bands incident to the ground measured by ASD Fieldspec pro tended to be more stable than the data measured by sunlight sensor of P4 Multispectral.

B. Calculation of Reflectance of Each Tarps

Table 6 shows the tarp reflectance calculated by direct measurement with a spectroradiometer.

Table 6 The reflectance of tarps calculated using spectroradiometer data

Reflectance of tarps	3%	23%	31%	46%
B	2.7	20.9	31.5	46.1
G	2.7	19.7	30.5	45.4
R	2.8	18.4	29.3	44.7
N	3.0	17.1	28.2	45.6

The reflectance was calculated based on the spectroradiometer measurements at four points on the tarp, using ground irradiance, and then averaged. Based on the known reflectance, the reflectance of each tarps was calculated in the UAV images.

The tarps were captured at the nadir once each in a total of five flights. Among the irradiance measured by two methods, the reflectance of the tarp in the nadir image was calculated using the spectroradiometer data, because the irradiance data measured by the sunlight sensor did not have a stable value and could not be used to calculate reflectance. Additionally, the check image was acquired at the same flight altitude as when the image was taken in the nadir, and the reflectance of the check image was calculated to verify the result of the reflectance calculation. The calculated reflectance of the tarp is shown in Table 7.

Table 7 The reflectance of tarps from UAV images calculated using irradiance data measured by spectroradiometer with RCR (unit: %)

		1st-3%	2nd-46%	3rd-23%	4th-46%	5th-31%
Nadir	B	2.0	45.6	19.1	45.0	25.9
	G	2.2	46.4	17.7	45.4	25.6
	R	2.1	46.4	15.8	45.0	22.5
	RE	1.8	46.6	12.8	44.4	17.4
	N	1.2	42.4	10.8	49.7	20.7
Avg	B	2.3	46.0	19.4	45.9	20.7
	G	2.4	46.9	18.1	46.2	26.4
	R	2.4	46.9	16.3	45.8	26.0
	RE	2.2	46.9	13.4	44.8	22.9
	N	1.7	43.4	11.7	50.8	17.6
Check	B	0.2	2.9	1.4	3.0	1.8
	G	0.3	2.9	1.2	3.0	1.6
	R	0.3	2.9	1.1	2.8	1.4
	RE	0.4	1.5	1.2	1.4	0.9
	N	0.5	3.6	1.5	3.6	2.0

2. BRDF Estimation and Analysis

A. ANIF Calculation

The ANIF value was calculated by obtaining the reflectance for each image, before and after correcting the ground irradiance, respectively. Figure 17 shows the calculated results, where 'Before ground irradiance correction' was calculated from an image without ground irradiance correction, and 'After ground irradiance correction' was calculated from an image with ground irradiance correction. ANIF results were calculated

with only 151 BRDF(hemispherical) images and the nadir images, excluding the check images. Figure 16 is a template explaining the results shown in Figure 17, which intuitively explains the ANIF calculation results at each azimuth angle and zenith angle.

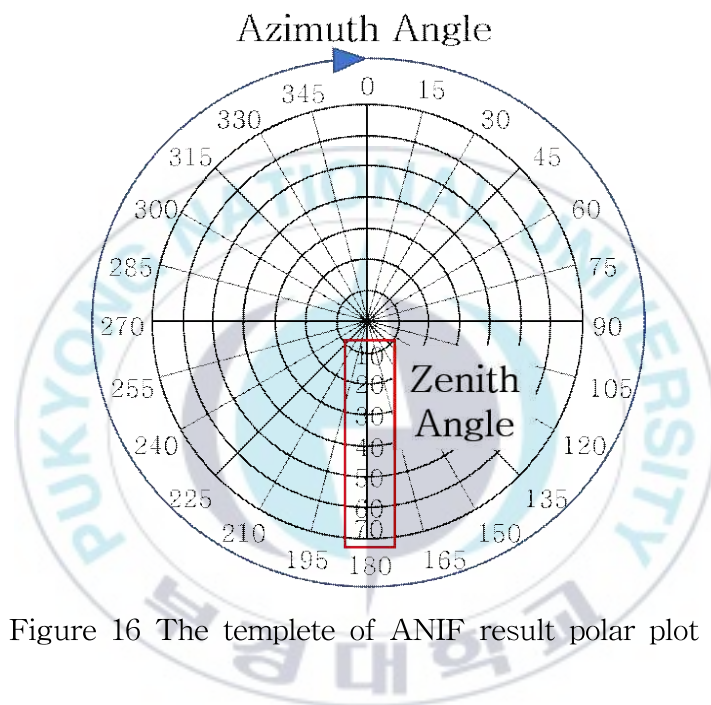


Figure 16 The template of ANIF result polar plot

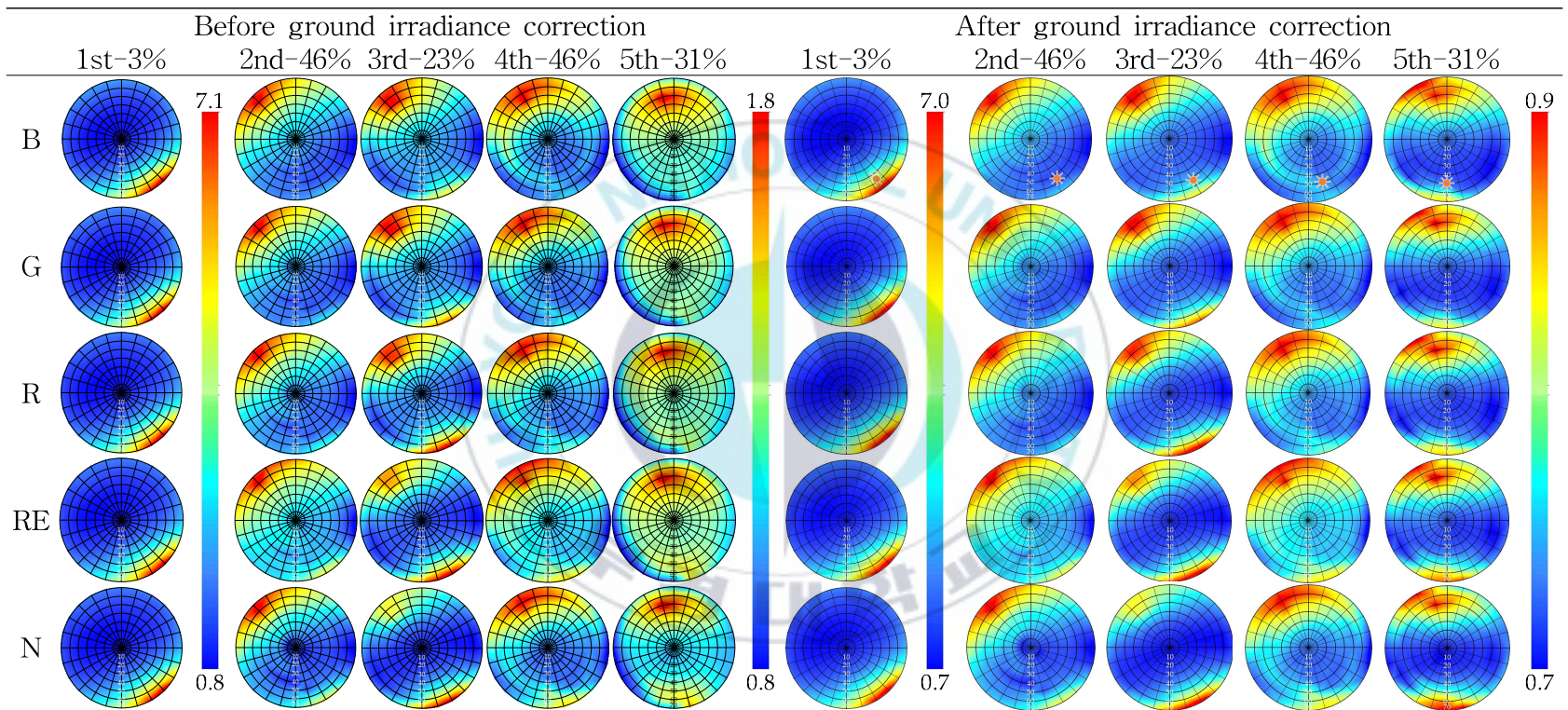


Figure 17 The ANIF results before and after irradiance correction

B. Calculation of the k value of the BRDF Model

The k value included in the BRDF formula was calculated using the ANIF data before and after ground irradiance correction. The k value was calculated differently according to the irradiance correction, as shown in Table 8, where 'B' data were calculated based on the ANIF results before correcting ground irradiance, and 'A' data were calculated based on the ANIF results before correcting ground irradiance. A BRDF model was created using the calculated k value, and through this, the reflectance at an arbitrary time can be simulated.

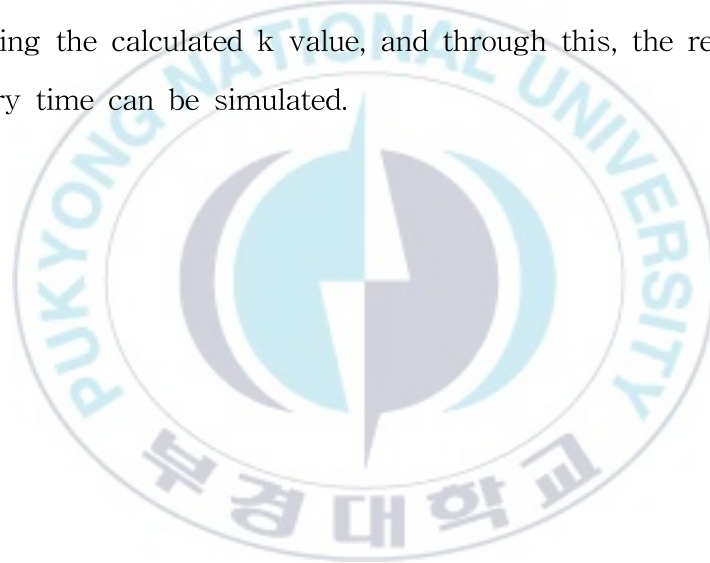


Table 8 The k value of BRDF model calculated in this study

Band	1st-3%			2nd-46%			3rd-21%			4th-46%			5th-31%			
	iso	vol	geo	iso	vol	geo	iso	vol	geo	iso	vol	geo	iso	vol	geo	
B	0.06	1.70	-0.59	1.05	0.41	0.09	1.15	0.51	0.07	1.14	0.45	0.08	1.51	0.01	0.19	
G	-0.01	1.71	-0.65	1.07	0.44	0.08	1.13	0.60	0.03	1.13	0.46	0.08	1.55	-0.06	0.20	
B	R	-0.16	1.89	-0.74	1.06	0.46	0.07	1.07	0.72	0.00	1.11	0.45	0.07	1.53	-0.03	0.19
RE	2.56	-0.99	1.01	0.26	0.03	1.00	1.08	-0.05	1.03	0.27	0.02	1.50	-0.06	0.16	2.56	
N	-1.85	5.13	-1.96	1.04	0.79	0.05	0.81	1.88	-0.19	1.09	0.66	0.04	1.39	0.50	0.12	
B	0.04	1.96	-0.67	1.16	0.33	0.09	1.16	0.36	0.09	1.16	0.42	0.09	1.15	0.39	0.08	
G	-0.04	1.97	-0.73	1.16	0.33	0.08	1.16	0.36	0.08	1.15	0.43	0.08	1.14	0.40	0.07	
A	R	-0.22	2.19	-0.84	1.13	0.33	0.07	1.13	0.36	0.07	1.12	0.42	0.07	1.12	0.39	0.06
RE	-0.63	2.95	-1.13	1.05	0.19	0.03	1.05	0.21	0.03	1.04	0.24	0.02	1.04	0.22	0.02	
N	-1.95	5.36	-2.03	1.12	0.50	0.05	1.12	0.54	0.05	1.11	0.63	0.04	1.10	0.60	0.03	

The reflectance is simulated after applying the calculated k value to the BRDF model, and then, inputting SAA, and SZA of the research data collection time.

When calculating the reflectance from the hemispherical images acquired in this study, the reflectance was calculated before and after correcting the ground irradiance for each images. The difference in reflectance before and after correcting the calculated reflectance and irradiance by inputting the image acquisition conditions(SAA and SZA) to the previously created BRDF model was calculated. The results are shown in Table 9.

Table 9 The difference between simulated reflectance and calculated reflectance before and after irradiance correction (unit: %)

		1st-3%	2nd-46%	3rd-21%	4th-46%	5th-31%	
B	BRDF	B	0.9	2.8	1.7	5.9	3.5
		G	1.2	3.3	1.9	7.0	3.9
		R	1.4	3.6	2.2	7.3	3.9
		RE	1.7	3.3	2.7	7.8	3.1
		N	2.6	4.9	4.2	9.0	5.3
	Check	B	0.3	4.7	3.0	1.4	1.8
		G	0.3	5.6	3.4	1.5	1.9
		R	0.3	6.1	3.3	1.8	1.9
		RE	0.4	5.5	2.7	1.7	1.5
		N	0.6	8.2	2.6	1.8	2.8
A	BRDF	B	1.1	1.8	1.5	2.7	2.2
		G	1.3	1.9	1.7	2.3	2.1
		R	1.5	2.1	2.0	2.6	2.2
		RE	1.9	1.8	2.5	1.9	1.7
		N	2.6	3.5	4.1	4.3	4.5
	Check	B	0.3	2.6	3.0	1.1	1.1
		G	0.3	3.0	2.5	1.0	1.2
		R	0.4	3.7	2.5	1.3	1.2
		RE	0.4	2.2	2.9	0.9	0.9
		N	0.5	5.9	4.1	2.0	2.6

The smaller the difference between the reflectance simulated by the BRDF and the calculated reflectance, the greater the accuracy. The ANIF results of the data simulated by the BRDF model are shown in Figure 15.



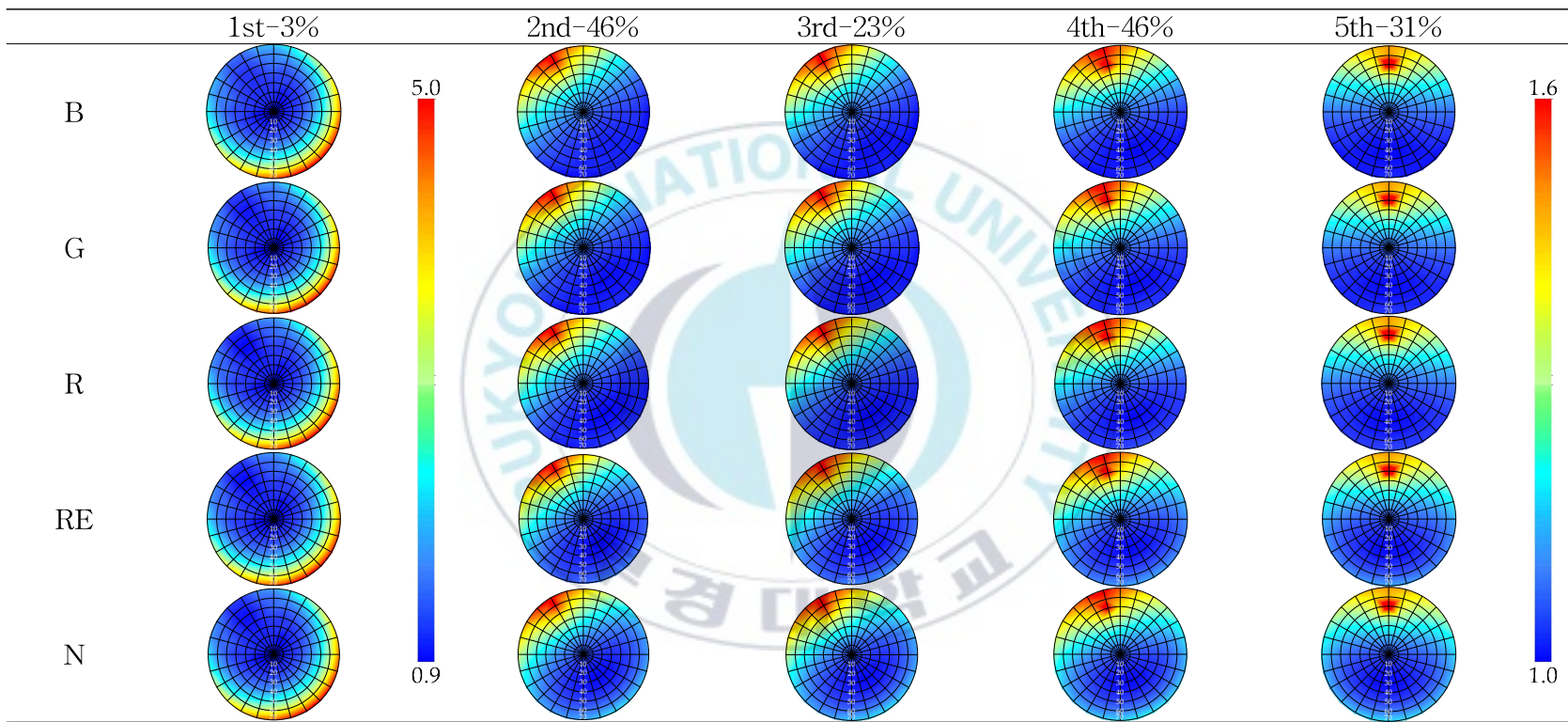


Figure 18 The ANIF results simulated by BRDF model estimated after irradiance correction

C. Homogeneity Analysis to Determine tarp Accuracy

The orthophotos of each tarp were preprocessed for reflectance calculations. To determine the accuracy of the tarp itself, it was calculated how homogeneously the tarp was installed. The results are shown in Table 10.

Table 10 The uncertainty of each tarps according to homogeneously

		1st-3%	2nd-46%	3rd-21%	4th-46%	5th-31%
BRDF	B	0.02	1.84	0.36	1.61	0.81
	G	0.02	2.07	0.38	1.75	0.87
	R	0.02	2.30	0.40	1.98	0.93
	RE	0.03	2.76	0.44	2.21	1.50
	N	0.04	3.31	0.60	3.13	1.64
Check	B	0.02	1.84	0.36	1.61	0.74
	G	0.03	2.12	0.40	1.79	0.81
	R	0.03	2.35	0.42	1.93	0.87
	RE	0.04	2.67	0.46	2.30	0.96
	N	0.05	3.50	0.64	3.08	1.58

The uncertainty of the data is explained based on the homogeneity of the tarp installed, which appeared to be 0.026% (BRDF image) and 0.034% (Check image) on average for the tarp homogeneity of 3%. Additionally, for the 20%, 32%, and 46% tarps in the BRDF image, the average uncertainties were 0.436%, 1.150%, and 2.296%, respectively. In the check images, they were 0.456%, 0.992%, and 2.319%, respectively. Overall, 46% of tarps showed high uncertainty.

IV. Conclusion

A UAV was used for the BRDF analysis, which is a significant indicator for identifying the anisotropic reflection characteristics of the ground surface. The UAV was operated in a hemispherical shape like a traditional field goniometer to capture the targets, and the spectroscopic image was acquired through a multispectral camera to determine the reflectance distribution characteristics for each band. It was possible to increase portability and efficiency by reducing the size and weight, which are significant disadvantages of traditional goniometers. However, when the sunlight sensor of UAV measured the irradiance required to calculate the reflectance of the target, the measured value was affected by the attitude changes of the UAV while it operated in a hemispherical shape. Therefore, a spectroradiometer was installed on the ground to obtain a more stable irradiance. After pre-processing the image acquired by UAV, the reflectance was calculated for the case in which the DN of each image was corrected with ground irradiance and in which no correction was made. When the nadir and check images were calibrated with the data obtained through these processes, it was identified that the reflectance had similar values. The ANIF—a value normalized by reflectance at the nadir—was calculated based on the calculated reflectance. The results showed different values for the cases before and after ground irradiance correction: Although the ANIF result prior to correction appeared

unstable, it had relatively stable reflection distribution characteristics after correction. When the k value of the BRDF model was calculated based on the results before and after ground irradiance correction, the k value showed a smaller standard deviation when using the result after correction compared to the case using the result prior to correction. When the reflection characteristics of each tarp were calculated at SAA and SZA of the time of data collection through the estimated BRDF model, the simulated results were found to be similar to those obtained when ground irradiance was corrected. As the BRDF analysis using a UAV goniometer showed similar accuracy as when using a traditional goniometer, it can be concluded that this study presents a method with increased time efficiency and portability. However, there is a limitation that a stable irradiance value must be measured on the ground because of a problem with the irradiance measuring sensor of the UAV. It should also be noted that accuracy may vary depending on the homogeneity of the surface on which the tarps are installed.

V. References

Abdou, W. A., M. C. Helmlinger, J. E. Conel, C. J. Bruegge, S. H. Pilorz, J. V. Martonchik, and B. J. Gaitley, 2001. Ground measurements of surface BRF and HDRF using PARABOLA III. *Journal of Geophysical Research: Atmospheres*, 106(D11): 11967–11976. <https://doi.org/10.1029/2000JD900654>

Aebischer, P., M. Sutter, and B. Reidy, 2020. Measuring sward height and dry matter yield of pastures using multispectral imagery from UAV and a random forest algorithm. *DIGICROP 2020*. 1.-10. Online.

ASD Expert Tip: What is a remote cosine receptor and when would I use it? – Materials Talks. (2020, May 6). <https://www.materials-talks.com/asd-expert-tip-what-is-a-remote-cosine-receptor-and-when-would-i-use-it/>

Bachmann, C. M., A. Abelev, M. J. Montes, W. Philpot, D. Gray, K. Z. Doctor, R. A. Fusina, G. Mattis, W. Chen, S. D. Noble, C. Coburn, T. Corl, L. Slomer, C. R. Nichols, E. Roggen, R. J. Hughes, S. Carr, S. Kharabash, A. Brady, and M. Vermillion, 2016. Flexible field goniometer system: The

Goniometer for Outdoor Portable Hyperspectral Earth Reflectance. *Journal of Applied Remote Sensing*, 10(3): 036012. <https://doi.org/10.1117/1.JRS.10.036012>

Berry, T. E., J. C. Morgan, J. S. Furey, T. A. DeMoss, J. R. Kelley and J. R. McKenna, 2012. Extensive goniometric spectral measurements at desert sites for military engineering, *Proc. of Reflection, Scattering, and Diffraction from Surfaces III*, San Diego, California, United States, Aug. 12–16, vol. 8495, pp. 286–299. <https://doi.org/10.1117/12.930217>

Bialek, A., C. Greenwell, M. Lamare, A. Meygret, S. Marcq, S. Lachérade, E. Woolliams, B. Berthelot, M. Bouvet, M. King, C. Underwood and N. Fox, 2016. New radiometric calibration site located at Gobabeb, Namib desert, *Proc. of 2016 IEEE International Geoscience and Remote Sensing Symposium (IGARSS)*, Beijing, China, Jul. 10–15, pp. 6094–6097. <https://doi.org/10.1109/IGARSS.2016.7730592>

Bihlmaier, A., F. Stein, and H. Wörn, 2016. Towards a generic BRDF/BTF measurement system: Improving visual realism in robot simulators using robots, *Proc. of 2016 IEEE International Conference on Emerging Technologies and Innovative Business Practices for the Transformation of Societies (EmergiTech)*, Balaclava, Mauritius, pp.

410-416. <https://doi.org/10.1109/EmergiTech.2016.7737376>

Bréon, F.-M., F. Maignan, M. Leroy, and I. Grant, 2002. Analysis of hot spot directional signatures measured from space, *Journal of Geophysical Research: Atmospheres*, 107(D16): AAC 1-1-AAC 1-15. <https://doi.org/10.1029/2001JD001094>

Bruegge, C. J., C. Coburn, A. Elmes, M. C. Helmlinger, F. Kataoka, M. Kuester, A. Kuze, T. Ochoa, C. Schaaf, K. Shiomi and F. M. Schwandner, 2019. Bi-Directional Reflectance Factor Determination of the Railroad Valley Playa, *Remote Sensing*, 11(22): 1-15. <https://doi.org/10.3390/rs11222601>

Byford, N. and Coburn, C. A., 2022. Temporal Variation in Surface Bidirectional Reflectance of the Railroad Valley Vicarious Calibration Test Site in Nevada, *Canadian Journal of Remote Sensing*, 48(6): 722-736. <https://doi.org/10.1080/07038992.2022.2114439>

Chang, Y., Z. Jiao, X. Zhang, L. Mei, Y. Dong, S. Yin, L. Cui, A. Ding, J. Guo, R. Xie, Z. Zhu and S. Li, 2021. Assessment of Improved Ross - Li BRDF Models Emphasizing Albedo Estimates at Large Solar Angles

Using POLDER Data, *IEEE Transactions on Geoscience and Remote Sensing*, 59(12): 9968–9986. <https://doi.org/10.1109/TGRS.2020.3030948>

Coburn, C. A., and D. R. Peddle, 2006. A low-cost field and laboratory goniometer system for estimating hyperspectral bidirectional reflectance. *Canadian Journal of Remote Sensing*, 32(3): 244–253. <https://doi.org/10.5589/m06-021>

Creasy, M. B., W. T. Tinkham, C. M. Hoffman, and J. C. Vogeler, 2021. Potential for individual tree monitoring in ponderosa pine dominated forests using unmanned aerial system structure from motion point clouds. *Canadian Journal of Forest Research*, 51(8): 1093–1105. <https://doi.org/10.1139/cjfr-2020-0433>

DALL, J. A., 1991. A Perfect Base for a GIS: The Digital Orthophoto. *Proc. of Civil Engineering Applications of Remote Sensing and Geographic Information Systems*. Washington, D.C., United States, May. 14–16., pp. 319–327.

Dangel, S., M. M. Verstraete, J. Schopfer, M. Kneubuhler, M. Schaepman, and K. I. Itten, 2005. Toward a direct comparison of field and laboratory

goniometer measurements. *IEEE Transactions on Geoscience and Remote Sensing*, 43(11): 2666–2675.
<https://doi.org/10.1109/TGRS.2005.857324>

DJI, P4 Multispectral – Specifications. Available online:
<https://www.dji.com/p4-multispectral/specs> (accessed on 22 July 2022a).

DJI, P4_Multispectral_Image_Processing_Guide_EN.Pdf. Available online:
https://dl.djicdn.com/downloads/p4-multispectral/20200717/P4_Multispectral_Image_Processing_Guide_EN.pdf (accessed on 9 February 2022b).

Doctor, K. Z., C. M. Bachmann, D. J. Gray, M. J. Montes, and R. A. Fusina, 2015. Wavelength dependence of the bidirectional reflectance distribution function (BRDF) of beach sands. *Applied Optics*, 54(31), F243–F255. <https://doi.org/10.1364/AO.54.00F243>

Gao, F., X. Li, A. Strahler, and C. Schaaf 2000. Evaluation of the Li transit kernel for BRDF modeling. *Remote Sensing Reviews*, 19(1–4), 205–224. <https://doi.org/10.1080/02757250009532419>

Gašparović, M., and L. Jurjević, 2017. Gimbal Influence on the Stability of Exterior Orientation Parameters of UAV Acquired Images. *Sensors*, 17(2), 1–16. <https://doi.org/10.3390/s17020401>

Huang, X., Z. Jiao, Y. Dong, H. Zhang, and X. Li, 2013. Analysis of BRDF and Albedo Retrieved by Kernel-Driven Models Using Field Measurements. *IEEE Journal of Selected Topics in Applied Earth Observations and Remote Sensing*, 6(1), 149–161. <https://doi.org/10.1109/JSTARS.2012.2208264>

Jain, K., and A. Pandey, 2021. Calibration of Satellite Imagery with Multispectral UAV Imagery. *Journal of the Indian Society of Remote Sensing*, 49(3), 479–490. <https://doi.org/10.1007/s12524-020-01251-z>

Jensen, J. R., and S. R. Schill, 2000. Bidirectional Reflectance Distribution Function (BRDF) Characteristics of Smooth Cordgrass (*Spartina alterniflora*) Obtained Using a Sandmeier Field Goniometer. *Geocarto International*, 15(2), 23–30. <https://doi.org/10.1080/10106049908542149>

Jeong, H., H. Ahn, J. Park, H. Kim, S. Kim, Y. Lee, and C. Choi, 2015. Feasibility of Using an Automatic Lens Distortion Correction (ALDC)

Camera in a Photogrammetric UAV System. *Journal of the Korean Society of Surveying, Geodesy, Photogrammetry and Cartography*, 33(6), 475-483. <https://doi.org/10.7848/ksgpc.2015.33.6.475>

Jia, W., Y. Pang, R. Tortini, D. Schläpfer, Z. Li, and J.-L. Roujean, 2020. A Kernel-Driven BRDF Approach to Correct Airborne Hyperspectral Imagery over Forested Areas with Rugged Topography. *Remote Sensing*, 12(3), 1-33. <https://doi.org/10.3390/rs12030432>

Jiang, G.-M., and Z.-L. Li, 2008. Intercomparison of Two BRDF Models in the Estimation of the Directional Emissivity in MIR Channel From MSG1-SEVIRI Data. *Optics Express*, 16(23), 19310-19321. <https://doi.org/10.1364/OE.16.019310>

Jiao, Z., C. B. Schaaf, Y. Dong, M. Román, M. J. Hill, J. M. Chen, Z. Wang, H. Zhang, E. Saenz, R. Poudyal, C. Gatebe, F.-M. Bréon, X. Li, and A. Strahler, 2016. A method for improving hotspot directional signatures in BRDF models used for MODIS. *Remote Sensing of Environment*, 186, 135-151. <https://doi.org/10.1016/j.rse.2016.08.007>

Kim, S. J., and M. Pollefeys, 2008. Robust Radiometric Calibration and

Vignetting Correction. *IEEE Transactions on Pattern Analysis and Machine Intelligence*, 30(4), 562–576.
<https://doi.org/10.1109/TPAMI.2007.70732>

King, R. L., P. Pradhan, and M. S. Cox, 2001. Measuring reflectance of soil surface roughness with a field goniometer. *Proc. IGARSS 2001. Scanning the Present and Resolving the Future. Proceedings. IEEE 2001 International Geoscience and Remote Sensing Symposium (Cat. No.01CH37217)*, Sydney, NSW, Australia, Jul. 09–13, vol. 3, pp. 1273–1275. <https://doi.org/10.1109/IGARSS.2001.976816>

Maignan, F., F.-M. Bréon, and R. Lacaze, 2004. Bidirectional reflectance of Earth targets: Evaluation of analytical models using a large set of spaceborne measurements with emphasis on the Hot Spot. *Remote Sensing of Environment*, 90(2), 210–220.
<https://doi.org/10.1016/j.rse.2003.12.006>

Marks, A., C. Fragiaco, A. MacArthur, G. Zibordi, N. Fox, and M. D. King, 2015. Characterisation of the HDRF (as a proxy for BRDF) of snow surfaces at Dome C, Antarctica, for the inter-calibration and inter-comparison of satellite optical data. *Remote Sensing of Environment*, 158, 407–416. <https://doi.org/10.1016/j.rse.2014.11.013>

Narmilan, A., F. Gonzalez, A. S. A. Salgadoe, and K. Powell, 2022. Detection of White Leaf Disease in Sugarcane Using Machine Learning Techniques over UAV Multispectral Images. *Drones*, 6(9), 1-22. <https://doi.org/10.3390/drones6090230>

Nicodemus, F. E., J. C. Richmond, J. J. Hsia, I. W. Ginsberg, and T. Limperis, 1977. *Geometrical Considerations and Nomenclature for Reflectance*. National Bureau of Standards, US Department of Commerce, Washington, DC. 3-50.

Oh, J. H., Y. D. Eo, and C. N. Lee, 2006. A Photogrammetric Network and Object Field Design for Efficient Self-Calibration of Non-metric Digital Cameras. *Journal of the Korean Society of Surveying, Geodesy, Photogrammetry and Cartography*, 24(3), 281-288 (in Korean with English abstract).

Painter, T. H., B. Paden, and J. Dozier, 2003. Automated spectro-goniometer: A spherical robot for the field measurement of the directional reflectance of snow. *Review of Scientific Instruments*, 74(12), 5179-5188. <https://doi.org/10.1063/1.1626011>

Privette, J. L., T. F. Eck, and D. W. Deering, 1997. Estimating spectral albedo and nadir reflectance through inversion of simple BRDF models with AVHRR/MODIS-like data. *Journal of Geophysical Research: Atmospheres*, 102(D24), 29529–29542. <https://doi.org/10.1029/97JD01215>

Roosjen, P. P. J., J. G. P. W. Clevers, H. M. Bartholomeus, M. E. Schaepman, G. Schaepman-Strub, H. Jalink, R. Van der Schoor, and A. De Jong, 2012. A Laboratory Goniometer System for Measuring Reflectance and Emittance Anisotropy. *Sensors*, 12(12), 17358–17371. <https://doi.org/10.3390/s121217358>

Roujean, J.-L., M. Leroy, and P.-Y. Deschamps, 1992. A bidirectional reflectance model of the Earth's surface for the correction of remote sensing data. *Journal of Geophysical Research*, 97(D18), 20455–20468. <https://doi.org/10.1029/92JD01411>

Sakamoto, T., D. Ogawa, S. Hiura, and N. Iwasaki, 2022. Alternative Procedure to Improve the Positioning Accuracy of Orthomosaic Images Acquired with Agisoft Metashape and DJI P4 Multispectral for Crop Growth Observation. *Photogrammetric Engineering & Remote Sensing*,

88(5), 323–332. <https://doi.org/10.14358/PERS.21-00064R2>

Sandmeier, S. R., and K. I. Itten, 1999. A field goniometer system (FIGOS) for acquisition of hyperspectral BRDF data. *IEEE Transactions on Geoscience and Remote Sensing*, 37(2), 978–986. <https://doi.org/10.1109/36.752216>

Sandmeier, St., Ch. Müller, B. Hosgood, and G. Andreoli, 1998. Physical Mechanisms in Hyperspectral BRDF Data of Grass and Watercress. *Remote Sensing of Environment*, 66(2), 222–233. [https://doi.org/10.1016/S0034-4257\(98\)00060-1](https://doi.org/10.1016/S0034-4257(98)00060-1)

Schill, S. R., J. R. Jensen, G. T. Raber, and D. E. Porter, 2004. Temporal Modeling of Bidirectional Reflection Distribution Function (BRDF) in Coastal Vegetation. *GIScience & Remote Sensing*, 41(2), 116–135. <https://doi.org/10.2747/1548-1603.41.2.116>

Schopfer, J. T., Dangel, S., Kneubühler, M., & Itten, K. I. (2007). Dual field-of-view goniometer system FIGOS. *Proc. ISPRS Working Group VII/1 Workshop ISPRSRS'07: "Physical Measurements and Signatures in Remote Sensing"*, Davos, Switzerland, Mar. 12–14, vol. XXXVI-7/C50,

pp. 1-6. <https://doi.org/10.5167/UZH-77996>

Smith, G. S., 1995. Digital Orthophotography and GIS, *Proc. of 1995 Esri International User Conference*, California, May. 22-26.

Tinkham, W. T., and N. C. Swayze, 2021. Influence of Agisoft Metashape Parameters on UAS Structure from Motion Individual Tree Detection from Canopy Height Models. *Forests*, 12(2), 1-14. <https://doi.org/10.3390/f12020250>

Vierling, L. A., D. W. Deering, and T. F. Eck, 1997. Differences in arctic tundra vegetation type and phenology as seen using bidirectional radiometry in the early growing season. *Remote Sensing of Environment*, 60(1), 71-82. [https://doi.org/10.1016/S0034-4257\(96\)00139-3](https://doi.org/10.1016/S0034-4257(96)00139-3)

Wanner, W., X. Li, and A. H. Strahler, 1995. On the derivation of kernels for kernel-driven models of bidirectional reflectance. *Journal of Geophysical Research: Atmospheres*, 100(D10), 21077-21089. <https://doi.org/10.1029/95JD02371>

Yeom, J.-M., K.-S. Han, and Y.-S. Kim, 2005. A Reflectance Normalization Via BRDF Model for the Korean Vegetation using MODIS 250m Data. *Korean Journal of Remote Sensing*, 21(6), 445-456 (in Korean with English abstract). <https://doi.org/10.7780/kjrs.2005.21.6.445>

Yu, J. J., S.-W. Son, H.-S. Park, H.-J. Jeon, and J.-H. Yoon, 2017. Evaluation of DSM Accuracy Based on UAS with Respect to Camera Calibration Methods and Application of Interior Orientation Parameters. *Korean Journal of Remote Sensing*, 33(5_3), 787-798 (in Korean with English abstract). <https://doi.org/10.7780/KJRS.2017.33.5.3.3>

Zhang, X., Z. Jiao, Y. Dong, H. Zhang, Y. Li, D. He, A. Ding, S. Yin, L. Cui, and Y. Chang, 2018. Potential Investigation of Linking PROSAIL with the Ross-Li BRDF Model for Vegetation Characterization. *Remote Sensing*, 10(3), 1-24. <https://doi.org/10.3390/rs10030437>

Zheng, Y., S. Lin, C. Kambhamettu, J. Yu, and S. B. Kang, 2009. Single-Image Vignetting Correction. *IEEE Transactions on Pattern Analysis and Machine Intelligence*, 31(12), 2243-2256. <https://doi.org/10.1109/TPAMI.2008.263>

Zhou, J., B. Wang, J. Fan, Y. Ma, Y. Wang, and Z. Zhang, 2022. A Systematic Study of Estimating Potato N Concentrations Using UAV-Based Hyper- and Multi-Spectral Imagery. *Agronomy*, 12(10), 1-16. <https://doi.org/10.3390/agronomy12102533>

